Z. Phys. Chem. **223** (2009) 1359–1377 / **DOI** 10.1524/zpch.2009.6084

Li Ion Diffusion in Nanocrystalline and Nanoglassy $LiAlSi_2O_6$ and $LiBO_2$ - Structure-Dynamics Relations in Two Glass Forming Compounds

By Alexander Kuhn*, Esther Tobschall‡, and Paul Heitjans**

Institut für Physikalische Chemie und Elektrochemie, and Zentrum für Festkörperchemie und Neue Materialien, Callinstr. 3–3a, 30167 Hannover, Germany

Dedicated to Prof. Dr. Klaus Funke on the occasion of his 65th birthday

(Received September 11, 2009; accepted October 6, 2009)

Ion Diffusion / Nanocrystalline / Nanoglassy / $LiAlSi_2O_6$ / $LiBO_2$

In the present study the Li diffusivity in nanostructured samples of two glass forming model systems, spodumene ($LiAlSi_2O_6$) and lithium metaborate ($LiBO_2$), was examined using ^{7}Li nuclear magnetic resonance (NMR) spin-lattice relaxometry and dc conductivity measurements. The nanostructured samples were prepared by high-energy ball milling of the respective crystalline starting material on the one hand and the corresponding glass on the other hand. The diffusivity of the glass exceeds that of the crystalline sample for both systems. However, when the crystalline samples are mechanically treated by ball milling the diffusivity is enhanced. Nevertheless, the diffusivity of these nanocrystalline samples remains lower than that of the corresponding glass. Surprisingly, when the glassy samples are treated in the same way the diffusivity decreases. After sufficiently long milling times the diffusivity of these nanoglassy samples approaches that of the nanocrystalline samples. This convergence effect seems to be due to structural relaxation processes as is suggested by supplementary infrared spectroscopy and ^{27}Al, ^{12}B magic angle spinning NMR measurements.

1. Introduction

In the last decades nanostructured materials have gained intense and ever growing interest [1]. Nanostructured materials show a great variety of properties in

* Corresponding author. E-mail: kuhn@pci.uni-hannover.de

** Corresponding author. E-mail: heitjans@pci.uni-hannover.de

‡ Present address: Technische Informationsbibliothek Hannover, Welfengarten 1b, 30167 Hannover, Germany

comparison with bulk materials even when the same chemical composition is considered (see, e.g., [2]). This opens up a wide field of new materials for different applications, e.g. as catalysts [3], sensors [4], adsorbents [5], advanced ceramics [6, 7] or as electrodes and electrolytes in secondary Li batteries [8, 9]. While the properties of single crystalline materials should be independent of the synthesis route, this is surely not the case for nanostructured materials which generally are metastable. The differing properties of, in particular, nanocrystalline materials in comparison with single crystalline ones are mainly attributed to the high volume fraction of interfacial regions [10] which increases with decreasing crystallite size d according to $x_{\text{interface}} = 1-[(d-\delta)/d]^3$ where δ denotes the thickness of the interface. The interfacial structure is strongly dependent on the preparation method of the samples. When prepared by grinding, i.e. high-energy (HE) ball milling (a top-down technique), highly defective interfaces are expected while this is not necessarily the case for nanocrystalline materials obtained by other techniques, e.g., chemical vapor deposition or epitaxy methods (bottom-up techniques). Thus it is not surprising that for nanocrystalline materials of the same composition properties may differ significantly. It should be noted that not only the structural properties of the interface are important but also space-charge effects [11] may be significant. However, in our present case it will turn out that the experimental findings are explicable by considering only structural effects.

As pointed out above, the term 'nanocrystalline' is used widely and independently of the preparation method. The term 'nanoglassy' was introduced by Gleiter [12] for nanostructured noncrystalline materials, in that case prepared by a bottom-up technique (gas condensation). However, analogously to 'nanocrystalline', we use the term 'nanoglassy' also for our nanostructured noncrystalline materials prepared from the glass by the top-down technique HE ball milling.

As model systems in order to compare the nanocrystalline and the corresponding nanoglassy state with respect to their ion dynamics we here chose spodumene ($LiAlSi_2O_6$) and lithium metaborate $LiBO_2$. The glassy form is easily available from the melt [13–16] in both cases. By investigating the Li dynamics in the crystal and in the corresponding glass, being chemically identical but structurally different, it is possible to deduce some structural features which promote ionic motion. Comparisons between diffusivities in crystalline spodumene as well as other Li aluminosilicates and their respective glassy counterparts have been reported in [13, 14, 17- 25]. When nanostructured samples are considered, in addition to the two structural varieties glass and crystal many other samples of the same chemical composition but with a different structure can be prepared allowing new insights into the structure-dynamics relation in those systems. In earlier work by our group and others, ion dynamics in nanocrystalline materials was studied (for reviews see, e.g., [10, 16, 26]). It was found that in many cases ionic motion is faster in nanocrystalline materials prepared by HE ball milling than in the corresponding microcrystalline powders. Surprisingly, HE ball milling of the glassy materials has the opposite effect, i.e. a decrease of

the diffusivity, as has very recently been reported by us in either of the two compounds [16, 27]. In this paper we will point out the similarities of the two case studies which make it reasonable to assume that the findings represent a rather generic behavior which will show up also in other glass forming systems.

2. Experiment

2.1 Sample Preparation and Characterization

Glassy $LiAlSi_2O_6$ was provided by Schott Glaswerke (Germany) [14]. Appropriate amounts of Li_2CO_3, Al_2O_3 and SiO_2 were melted. The glass was obtained from the melt by roller quenching. The product turned out to be fully x-ray amorphous (Fig. 1a). Differential thermoanalysis (DTA) showed a second order phase transition at T_g = 960 K followed by an exothermal peak (crystallization) at 1120 K. Microcrystalline $LiAlSi_2O_6$ was prepared by devitrification of the glass. The crystallization process was completed after heating the glass sample for five days at 1270 K. X-ray diffraction (XRD) measurements of the crystalline sample confirmed the phase purity and revealed the typical pattern of microcrystalline β-spodumene [28]. XRD patterns were recorded with a Philips PW 1800 diffractometer (Bragg-Brentano geometry) using Cu K_α radiation.

Nanocrystalline $LiAlSi_2O_6$ was prepared by HE ball milling using a SPEX 8000 ball mill. An alumina (α-Al_2O_3, 99.5%) vial set with a single ball (10 mm in diameter) made of alumina was used. Alternatively, a ZrO_2 vial set was employed which led to the same results. The ball-to-powder weight ratio was about 4:1. The $LiAlSi_2O_6$ glass was mechanically treated under the same conditions. In both cases the milling time was varied from 1 h to 8 h. The ball milled samples were characterized by XRD and transmission electron microscopy (TEM). The average crystallite size was roughly estimated from the broadening of the three most intense XRD peaks utilizing the equation introduced by Scherrer [29] (cf. [10]). For both the micro- and the nanocrystalline sample the typical x-ray pattern of β-spodumene was obtained indicating that no phase transformation took place during milling, see Fig. 1a. The glassy $LiAlSi_2O_6$ as well as the corresponding ball milled samples were found to be completely x-ray amorphous (Fig. 1a). Abrasion of α-Al_2O_3 is unavoidable when the materials are milled in the alumina vial for longer times. However, small amounts of α-Al_2O_3 (approximately 5 wt% or less) were shown to have no effect on the Li conductivity here. Preliminary TEM images of the nanocrystalline samples seem to show crystalline particles embedded in an amorphous matrix of grain boundaries. For the mechanically treated glassy samples no indications of crystalline regions were found. The particle size estimated via TEM appears to be somewhat larger than the crystallite size which can be deduced via the Scherrer equation. This supports the conception of nanocrystallites being cluster assembled. The samples are only very weakly hygroscopic. After being kept under air for several months, thermo-

gravimetry (TG) measurements showed a water content of less than 2%. In infrared (IR) spectra of fresh samples prepared under ambient air, there are no indications of any moisture.

Microcrystalline $LiBO_2$ (99.995%, Aldrich Chemical Co.) was used as a starting material for the nanocrystalline samples. XRD measurements using a Philips PW 1050 (Bragg-Brentano geometry) showed that the delivered powder was a mixture of the main component α-$LiBO_2$, γ-$LiBO_2$ (20% or less) and some $Li_2B_4O_7$ (Fig. 1b). The $LiBO_2$ glass was prepared from Li_2CO_3 and B_2O_3. Appropriate amounts of these educts were ground in a ball mill and then melted in a platinum crucible (1325 K, 20 min). The melt was quenched between two polished copper plates. The glass was found to be fully x-ray amorphous and showed the expected molar ratio of Li:B = 1:1 as confirmed by inductively coupled plasma atomic emission spectroscopy (ICP-AES, performed by the Forschungszentrum Jülich). DTA measurements were done using a Netzsch STA 429. In the DTA curves (Fig. 2b), the glass transition is clearly seen at 700 K followed by an exothermal peak indicating crystallization at 780 K [15].

Nanocrystalline $LiBO_2$ was prepared using a SPEX 8000 ball mill as described above for $LiAlSi_2O_6$ with a ball-to-powder weight ratio of 1:1. The milling times were varied between 0.5 h and 48 h. After 10 h the crystallite size, calculated via the Scherrer equation (see above), was about 15 nm and was not reduced any further. It seems that only for α-$LiBO_2$ the crystallite size is reduced (as seen by a broadening of the XRD peaks, see Fig. 1) while the γ-$LiBO_2$ peaks in the XRD pattern remain unaltered by milling. Abrasion of alumina was not observed here. DTA measurements of the nanocrystalline samples (Fig. 2a) showed an exothermal peak at 710 K due to crystallization which increases with increasing milling time. This indicates a partial amorphization during milling, which results in nanocrystals embedded in an amorphous matrix [15]. The second, endothermic, peak visible in the DTA curves of nanocrystalline $LiBO_2$ in Fig. 2a is due to the transformation of the γ-$LiBO_2$, partially present in the sample, to α-$LiBO_2$ [15]. When milling the $LiBO_2$ glass, the ball-to-powder weight ratio had to be increased to 4:1 since there was only a small amount of the glass available. Thus, milling times are not directly comparable. For nanoglassy $LiBO_2$ as well, there were no signs of crystallization in the XRD measurements. DTA curves (Fig. 2b) show a decrease of the crystallization temperature down to 730 K with decreasing particle size, which makes it impossible to observe a glass transition in the ball milled samples. However, for short milling times it seems that the glass transition covers a broader temperature range and is less pronounced than in the unmilled glass, which might indicate a distribution of glass transition temperatures.

$LiBO_2$ is known to be rather hygroscopic. Therefore, all steps of the preparation and handling (except for the quenching of the glass) were performed under dry nitrogen atmosphere in a glove bag. Nevertheless, thermogravimetry (TG) as well as IR spectroscopy measurements showed a small amount of water (less than 2%) which was essentially equal for all samples. When the samples were

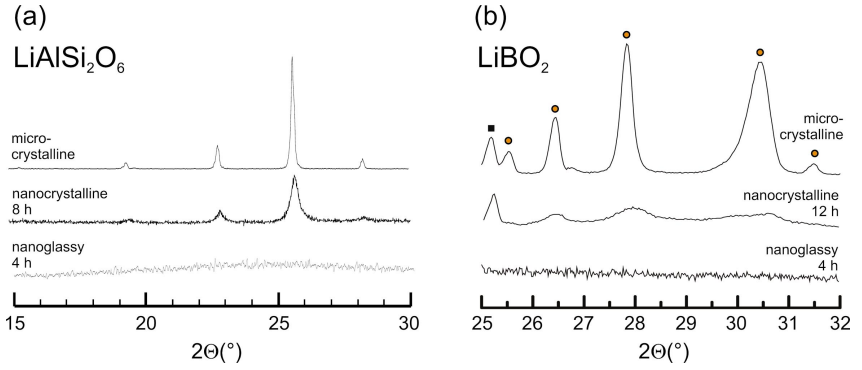

Fig. 1. (a) XRD patterns of micro- and nanocrystalline $LiAlSi_2O_6$. The coarse grained sample was prepared by devitrification of $LiAlSi_2O_6$ glass and subsequent extensive grinding of the specimen. The nanocrystalline sample was prepared by high-energy ball milling of the microcrystalline source material. For comparison, the XRD pattern of glassy $LiAlSi_2O_6$ mechanically treated for 4 h in the same shaker mill is also shown. (b) XRD patterns of the $LiBO_2$ samples. In the pattern of the microcrystalline sample, squares denote peaks of γ-$LiBO_2$ while the peaks of α-$LiBO_2$ are indicated by circles. The peak of γ-$LiBO_2$ is not altered during milling. The peaks of α-$LiBO_2$ are broadened during milling. As in $LiAlSi_2O_6$, the milled glassy sample is still amorphous.

intentionally kept under a water atmosphere, the hydration kinetics, measured via the increase of weight as a function of time, could be followed. Remarkably, the nanocrystalline sample showed exactly the same behaviour as the microcrystalline one. After 180 h, the weight of the samples had increased by 45%.

2.2 NMR, Impedance and IR Measurements - Technique and Setup

For the NMR measurements, a modified MSL 100 spectrometer (Bruker, Germany) was used. The radiofrequency pulses were amplified with a Kalmus LP 400 high-frequency power amplifier. A tunable Oxford cryomagnet (0 - 8 T) was used. Measurements were performed at a nominal field of 4.7 T for the $LiAlSi_2O_6$ samples and 1.5 T for the $LiBO_2$ samples corresponding to a ^{7}Li resonance frequency of about 77.7 MHz and 24.5 MHz, respectively. Measurements were carried out in the temperature range from 170 K to 490 K with a commercial Bruker probe. The temperature was controlled with an accuracy of 0.5 K using a gas flow of freshly evaporated nitrogen or a stream of heated air. ^{7}Li spin-lattice relaxation rates were determined using the conventional saturation recovery pulse sequence: $10\times90^\circ - t - 90^\circ$ – acq. A comb of closely spaced (50 μs) 90° pulses destroyed the equilibrium magnetization M_0. Its diffusion induced and thus temperature dependent recovery was followed as a function of delay time t. The 90° pulse length was about 5 μs. Magnetization transients showed single-exponential time behaviour $M(t) = M_0(1–\exp(-t/T_1))$ within ±10 %. They were recorded for 30 different t values. The longest delay time t

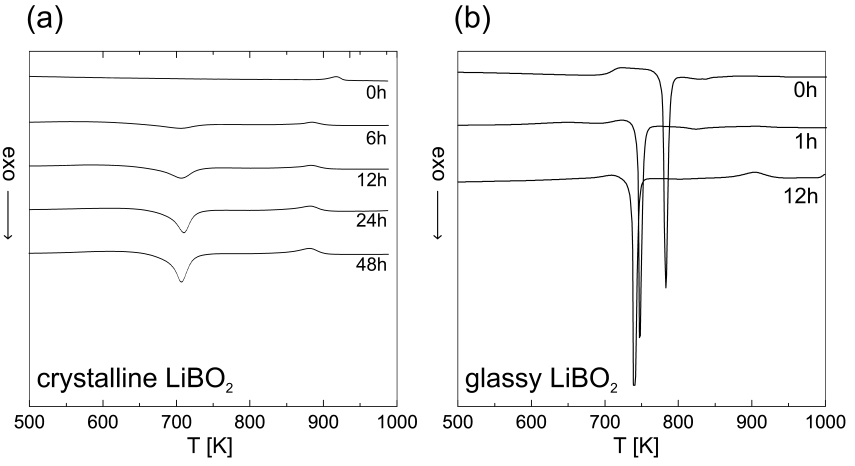

Fig. 2. (a) DTA curves of crystalline and nanocrystalline $LiBO_2$ with the respective milling times. With increasing milling time, an exothermic peak due to crystallization (compare with the DTA curve of the glass on the right) gets more and more pronounced indicating amorphization of the interfacial regions. (b) DTA curves of the glassy and the nanoglassy samples. In the DTA curve of the glass, the glass transition at 700 K is clearly seen, while this is not the case for the ball-milled samples. The crystallization peak at 780 K is shifted to lower temperatures during milling.

was set to at least 5 T_1. Each data point of $M(t)$ was obtained utilizing the integral over the free induction decay (FID). The ^{7}Li NMR spectra of $LiBO_2$ were obtained simply by a Fourier transformation of the equilibrium FID from the spin-lattice relaxation measurements. The ^{7}Li NMR spectra of $LiAlSi_2O_6$ were recorded with the solid-echo pulse sequence $90^\circ - t_e - 64^\circ$ – acq. (see, e.g., Ref. [31]) to avoid problems arising from dead time. The interpulse delay ranged from 10 to 20 μs. It should be noted that in the case of microcrystalline $LiBO_2$ NMR measurements were not possible in reasonable time (it took 2–3 days to measure one FID) due to the small ^{7}Li spin-lattice relaxation rate $1/T_1$. After 6 h of milling, $1/T_1$ was large enough to allow NMR measurements. ^{27}Al and ^{11}B magic angle spinning (MAS) NMR measurements were performed at room temperature using a commercial Bruker probe. Measurements were carried out at spinning rates of 10 kHz and 12 kHz in order to distinguish spinning sidebands.

Impedance measurements on both the nanocrystalline and nanoglassy samples were only performed for the model system $LiAlSi_2O_6$. Pellets for impedance measurements were prepared by conventional room temperature pressing of the ball milled powder under an uniaxial pressure of 1 GPa. Conductive carbon was used as electrode material. In the case of glassy $LiAlSi_2O_6$ thin specimens were prepared, which were polished before conductive carbon adhesive (Alfa Aesar) was applied. Alternatively, Au was used which led to the same results as already pointed out by Roth and Böhm [18]. However, Au did not adhere well to the

surface of the samples at higher temperatures. Impedance spectra were recorded with an HP 4192 A impedance analyzer. An alternating voltage of 100 mV amplitude was applied to the sample over a frequency range from ν = 10 Hz to 1 MHz. Conductivity jigs with a four terminal configuration were used. Impedance spectra were recorded between room temperature and 800 K in nitrogen atmosphere. At higher temperatures ($T > 800\ K$) significant grain growth of the nanocrystalline particles proceeds.

For IR absorbance spectroscopy measurements in the case of $LiBO_2$, pellets of 200 mg KBr and 2 mg of the samples were pressed. A pure KBr pellet was used as a reference. The spectra were recorded using a Bruker IFS66v/S IR spectrometer with an evacuated measurement chamber to reduce influences of carbon dioxide and water. For IR reflectance spectroscopy measurements, a Bruker Tensor 27 FT-IR spectrometer with the reflection angle set to 90° was used.

3. Results and discussion

3.1 NMR motional narrowing

The ^{7}Li NMR line at low temperatures in the so-called rigid lattice regime is determined by static dipolar interaction between the magnetic moments of the nuclei leading to a broad, often Gaussian shaped, line with a full width at half maximum (*fwhm*) in the order of usually some kHz. At higher temperatures when the ionic motional correlation rate becomes fast with respect to the rigid lattice fwhm, the NMR line narrows to a sharp, often Lorentzian shaped, line. The onset temperature of this effect called motional narrowing (MN) is a rough parameter to characterize the diffusivity in a material [32]. In Fig. 3a, the MN of the linewidth of the ^{7}Li NMR central transition, recorded at a frequency of $\omega\omega_0/2\pi$ = 77.7 MHz and normalized to the rigid lattice linewidth, is shown for glassy and crystalline $LiAlSi_2O_6$ as well as for the respective ball-milled samples (t_{mill} = 4 h). The rigid lattice linewidth $fwhm_{rigid\ lattice}$ varied between 3.5 kHz and 4 kHz (crystalline sample: 3.55 kHz, glassy sample: 3.65 kHz, ball milled samples: 3.8 - 4.0 kHz). The slightly higher value in the ball milled samples is probably due to a small amount of paramagnetic impurities introduced into the sample. There is no systematic correlation between the milling time and the rigid lattice linewidth in the ball milled samples; the variations between samples of the same milling time are of the same magnitude as those between samples of different milling times.

For $LiBO_2$ the ^{7}Li NMR spectra were recorded at a frequency of $\omega_0/2\pi$ = 24.5 MHz. As mentioned above, for $LiBO_2$ it was not possible to measure the microcrystalline sample in a reasonable time due to the long relaxation time. However, one spectrum was recorded at an elevated temperature (460 K, the highest temperature accessible with the probe used here). The central transition

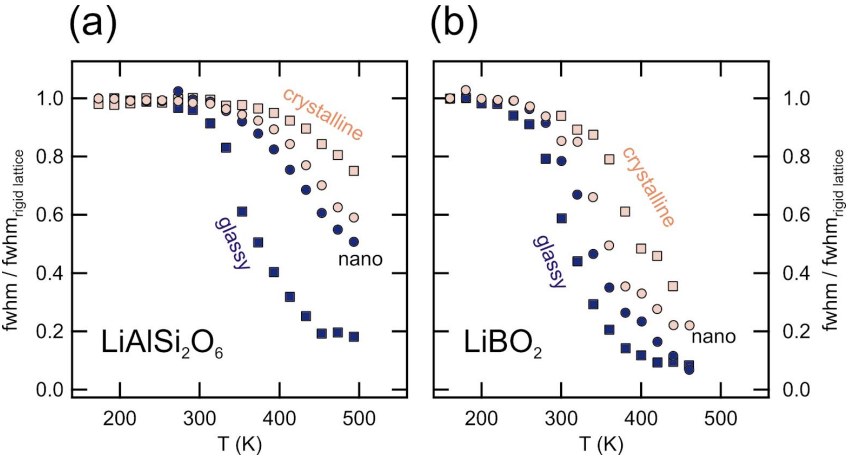

Fig. 3. (a) Motional narrowing (MN) of the normalized linewidths of the ^{7}Li NMR central transition of the $LiAlSi_2O_6$ samples recorded at $\omega_0/2\pi$ = 77.7 MHz. Dark squares: glassy sample, light squares: microcrystalline sample. The MN onset temperatures of the nanostructured samples (dark circles: nanoglassy; light circles: nanocrystalline) show intermediate values between those of the starting materials (after [27]). (b) MN of the ^{7}Li line of the $LiBO_2$ samples recorded at $\omega_0/2\pi$ = 24.5 MHz. Dark squares: glassy sample, light squares: nanocrystalline sample milled for 6 h. In the nanoglassy sample ball milled for 12 h (dark circles) the diffusivity is reduced while the opposite effect is found for the nanocrystalline sample ball milled for 24 h (light circles).

showed a *fwhm* of about 9 kHz which is still in the order of the rigid lattice linewidth of the other samples (about 10 kHz for the glassy and nanoglassy samples, about 11 kHz for the nanocrystalline sample ball milled for 24 h). In Fig. 3b the motional narrowing of glassy $LiBO_2$ and, instead of microcrystalline $LiBO_2$, that of the sample milled for 6 h are depicted. Additionally, the motional narrowing of the nanostructured samples referring to long milling times (t_{mill} = 12 h for the nanoglassy sample, t_{mill} = 24 h for the nanocrystalline sample) is shown.

Obviously both systems exhibit the same trend. The glassy samples show the highest and the crystalline samples show the lowest diffusivities. During milling, the diffusivity of the crystal is enhanced while the opposite effect is found for the glass resulting in a convergence of diffusivities during milling.

3.2 ^{7}Li NMR spin-lattice relaxation

^{7}Li NMR spin-lattice relaxation (SLR) rates ($1/T_1$) were measured for all samples in the temperature range from 140 K to 460 K. According to the BPP model [33] - a phenomenological model assuming isotropic, three-dimensional ionic motion - the NMR SLR rate is proportional to the jump rate and thus follows an Arrhenius temperature dependence $1/T_1 \propto \exp[-E_A/(k_B T)]$ at low temperatures,

when the Li jump rate τ^{-1} is much smaller than the Larmor frequency ω_0 of the NMR experiment. Here E_A is the activation energy and k_B Boltzmann's constant. At higher temperatures, when the jump rate τ^{-1} is in the range of ω_0, the NMR SLR rate does not increase any further but shows a maximum. From the maximum a (slightly model dependent) absolute jump rate τ^{-1} can be derived using the maximum condition $\omega_0 \cdot \tau = 1$. At even higher temperatures, when $\tau^{-1} >> \omega_0$, the SLR rate decreases with increasing temperature according to $1/T_1 \propto \exp[E_A/(k_B T)]$. In the ideal BPP case, the Arrhenius plot of the NMR SLR rates is symmetric and the activation energies of the low-temperature flank and the high-temperature flank are equal. However, if structural disorder is present, there may be a distribution of activation energies. In that case, the activation energy obtained from the low-temperature flank ($\tau^{-1} << \omega_0$), being according to its time scale sensitive to short-range motion, is smaller than that from the high-temperature flank ($\tau^{-1} >> \omega_0$) or that measured by other long-range sensitive methods such as dc conductivity (see, e.g., Ref. [23]).

In the present case the NMR SLR rates at still lower temperatures are determined by non-diffusion induced background relaxation which is, e.g., due to relaxation by lattice phonons and/or paramagnetic impurities. However, at higher temperatures (but still on the low-temperature flank, see Refs. [14,17]), the NMR SLR rates are diffusion induced and can thus be used to compare short-range diffusivities in a qualitative manner.

In Fig. 4 the diffusion induced ^{7}Li NMR SLR rates $1/T_{1,\mathrm{diff}}$ are shown in Arrhenius plots for the two model systems. For both $LiAlSi_2O_6$ and $LiBO_2$ the trend observed in the MN of the NMR lines (see Fig. 3) is found again. In the case of $LiAlSi_2O_6$ (Fig. 4a), the decrease of Li diffusivity in the glass during milling and the enhancing effect of milling in the crystalline material are clearly seen. We will call this 'convergence effect' in the following. The activation energies referring to short-range diffusivity amount to 0.32 eV in the glass and 0.38 eV in the crystal, and depend only slightly on the milling time. In the case of $LiBO_2$, the SLR rates follow the same general trend (Fig. 4b). As mentioned above, it was not possible to measure the microcrystalline sample. The sample with the shortest milling time which could be measured was that milled for 6 h. However, even for this sample the relaxation rates seem to be dominated by non-diffusion induced background relaxation. Still, the data was plotted in the diagram since the total relaxation rate $1/T_{1,\mathrm{total}}$ is always larger or equal to the diffusion induced relaxation rate: $1/T_{1,\mathrm{total}} = 1/T_{1,\mathrm{diff}} + 1/T_{1,\mathrm{background}} \geq 1/T_{1,\mathrm{diff}}$. In the temperature range shown in Fig. 4b the NMR SLR rates of all the other samples are diffusion induced. Their activation energies range from 0.21 eV to 0.23 eV and are only slightly affected by milling. Thus, the convergence effect seen in Fig. 4a for $LiAlSi_2O_6$ is also found for $LiBO_2$. It should be noted that the decrease of the NMR SLR rate in the nanoglassy samples is not due to abrasion of alumina for the following reasons. Firstly, concerning the background relaxation rate, abrasion of alumina or any other contamination, e.g. by paramagnetic ions, during milling is expected to lead to an increase rather than a decrease

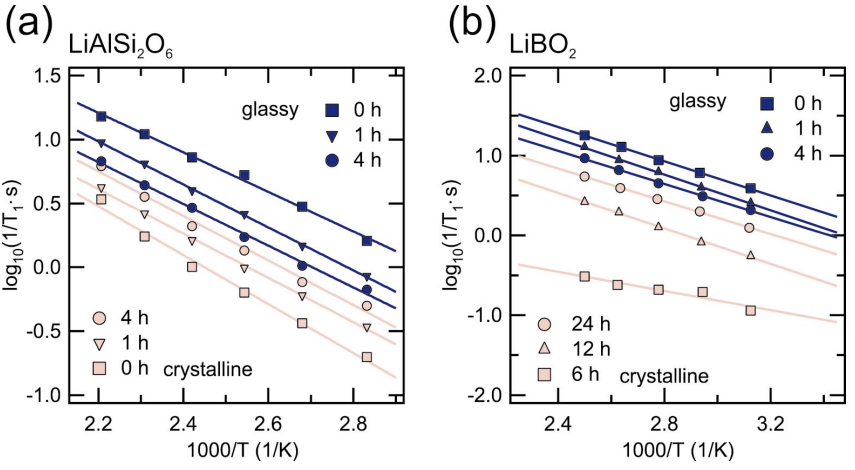

Fig. 4. (a) Diffusion induced ^{7}Li NMR spin-lattice relaxation (SLR) rates $1/T_{1,\mathrm{diff}}$ of the $LiAlSi_2O_6$ samples (milling time varied from 0 h to 8 h) recorded at $\omega_0/2\pi$ = 77.7 MHz. (b) ^{7}Li SLR rates of the $LiBO_2$ samples recorded at $\omega_0/2\pi$ = 24.5 MHz.

of the relaxation rate. Secondly, also the diffusion induced relaxation rate normally increases when an ionic insulator is admixed to an ionic conductor, thus forming a nanocrystalline composite with enhanced conductivity, as is known from previous work by our group on Li_2O-B_2O_3 and Li_2O-Al_2O_3 [34 - 39]. This was confirmed in the present study by intentionally adding nanocrystalline alumina (up to 75%) to nanoglassy $LiAlSi_2O_6$ which led to a slight increase of $1/T_1$ (by about 25%). Additionally, both glassy and crystalline spodumene were milled in a zirconia vial set where abrasion is minimized. The convergence effect was also found for these samples (measured by ^{7}Li NMR SLR and ^{7}Li NMR MN). So the decrease of the relaxation rates in the glassy samples during milling is most probably due to a decrease of diffusivity.

In Fig. 5 the 'convergence effect' is seen more clearly. Here, the ^{7}Li NMR SLR rates at a given temperature in the diffusion induced temperature range are shown as a function of the milling time. For both model systems the same general behavior is found. In crystalline $LiAlSi_2O_6$ (see Fig. 5a) the NMR SLR rate is increased by about a factor of 3 during milling while a reduction by the same factor is found for glassy $LiAlSi_2O_6$. In the case of crystalline $LiBO_2$ (Fig. 5b), the NMR SLR rate is increased by a factor of at least 30 when going from t_{mill} = 6 h to 24 h. Nevertheless, for glassy $LiBO_2$ the NMR SLR rate is reduced by a factor of 3 during milling which is the same value as found for $LiAlSi_2O_6$. This factor might represent the excess diffusivity which refers to the structure of the glass prepared by rapid cooling in comparison with the amorphous structures prepared at room temperature by HE ball-milling. When milling the crystalline materials, the diffusivity converges to a value which is by about a factor of 3

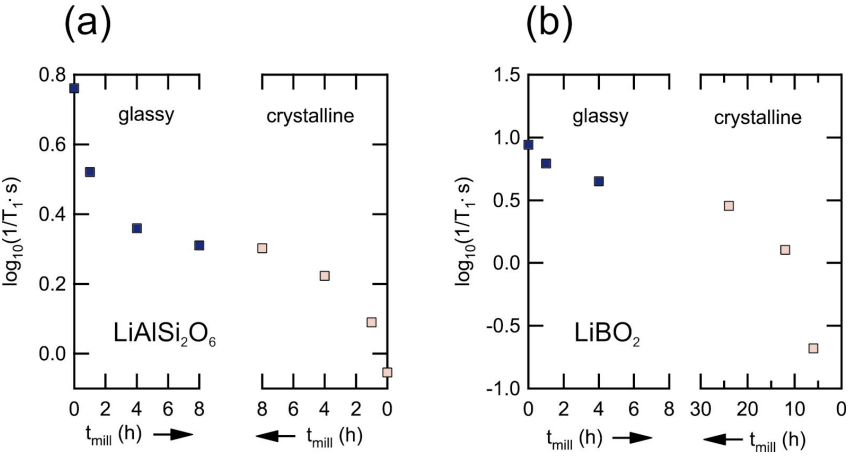

Fig. 5. (a) Diffusion induced ^{7}Li NMR spin-lattice relaxation (SLR) rates $1/T_{1,\mathrm{diff}}$ of the glassy (dark squares) and crystalline (light squares) $LiAlSi_2O_6$ samples as a function of milling time. Data were recorded at T = 393 K and $\omega_0/2\pi$ = 77.7 MHz. (b) Diffusion induced ^{7}Li NMR SLR rates $1/T_{1,\mathrm{diff}}$ of the glassy (dark squares) and crystalline (light squares) $LiBO_2$ samples as a function of milling time. Data were recorded at T = 360 K and $\omega_0/2\pi$ = 24.5 MHz.

smaller than that in the glass. In the case of $LiBO_2$ the diffusivity of the crystalline material converges after longer milling times than in the case of the glassy sample. This is due to a smaller ball-to-powder weight ratio (1:1 instead of 4:1, see section 2.1).

3.3 Impedance spectroscopy

As mentioned above, impedance spectroscopy measurements for both the nanocrystalline and the nanoglassy samples were only performed for $LiAlSi_2O_6$, and only the dc conductivity results of this model system will be dealt with here. The dc conductivity of nanocrystalline $LiBO_2$, which increases with increasing milling time similar to that of nanocrystalline $LiAlSi_2O_6$ (see below), has been reported in Ref. [16].

As indicated earlier, dc conductivities contain information about long-range diffusivity according to the time scale (5 Hz...10 kHz) of the measurement. The dc conductivity σ_{dc} is directly related to the long-range diffusion coefficient D_{dc} via the Nernst-Einstein relation $D_{\mathrm{dc}} = \sigma_{\mathrm{dc}} k_B T/(Nq^2)$. N and q denote the number density and the charge of the charge carrier, respectively. This equation is valid when the conductivity is only due to a thermally activated jumping process of one mobile ion species. In general, the temperature dependence of D_{dc}, and thus that of $\sigma_{\mathrm{dc}}T$, follows an Arrhenius law. In Fig. 6 the dc conductivities obtained from the dc plateau of the impedance spectra (real part of the conductivity σ' vs. the frequency ν) are displayed in an Arrhenius plot. Altogether the convergence effect pointed out in section 3.2 for the short-range diffusion induced NMR SLR

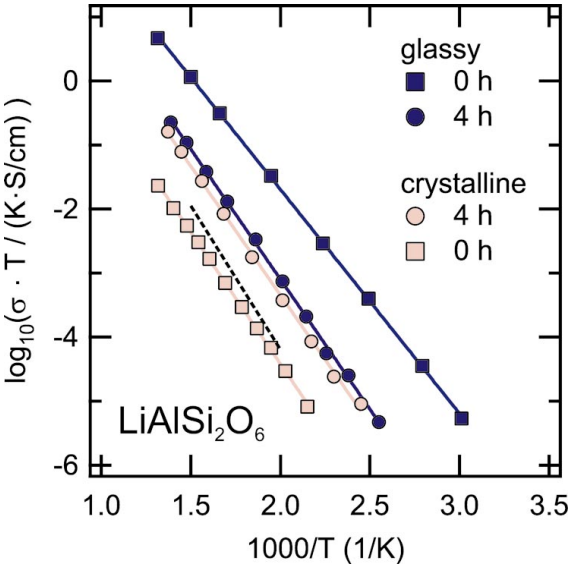

Fig. 6. DC conductivities of the $LiAlSi_2O_6$ samples (dark squares/circles: glassy/nanoglassy sample, light squares/circles: crystalline/nanocrystalline sample). For comparison, the conductivity of the single crystal, taken from [18] is displayed, too (dotted line). In milling the crystal and the glass, their diffusivities converge to the same intermediate value.

rate is also found for the dc conductivity of $LiAlSi_2O_6$. The glass sample shows the highest conductivity and the microcrystalline one the lowest conductivity while the nanostructured samples have intermediate conductivities. The dotted line represents the conductivity of a single crystal reported by Roth et al. [18]. The conductivity of the microcrystalline sample measured here is slightly lower. Obviously there are some blocking effects by the grain boundaries in this material. However, the conductivity of the glass we measured perfectly fits with that of Ref. [18]. The long-range activation energies are 0.82(1) eV for the microcrystalline sample and 0.69(1) for the glass. The activation energies of the nanostructured samples of 0.80(1) eV are nearly identical.

3.4 Structural investigations by ^{11}B, ^{27}Al MAS NMR and IR spectroscopy

In order to elucidate the structural changes that take place during milling, MAS NMR and IR spectra were measured for all samples. As already pointed out in the literature [28, 40, 41], both Si and Al in glassy $LiAlSi_2O_6$ as well as in crystalline $LiAlSi_2O_6$ in the β-modification have the same coordination polyhedra. Both Si and Al are tetrahedrally coordinated forming a three-dimensional network. The Li ions do not take part in that network but remain in the cages formed by the network compensating its negative charge. In Fig. 8a, ^{27}Al MAS

NMR spectra show that only tetrahedral Al (chemical shift $\delta \approx 50$ ppm) is present also in the ball milled samples indicating that the coordination does not change during milling. Expectedly, the ^{27}Al MAS NMR line of crystalline spodumene is narrower than that of the milled samples and the glass. During milling the ^{27}Al MAS NMR line of the crystalline sample is broadened which reflects the structural disorder introduced into the sample. Note that for the ^{27}Al MAS NMR measurements the samples were milled in a zirconia vial set in order to exclude influences of abraded alumina. These findings are corroborated by IR measurements. The IR reflectance spectrum (see Fig. 7a) of the crystalline sample shows at least three peaks of asymmetric SiO stretching vibration in tetrahedral SiO_4 units at 990 cm^{-1}, 1050 cm^{-1} and 1150 cm^{-1} and bending vibration modi at 700 cm^{-1} and 790 cm^{-1} which is in good agreement with IR absorbance spectra in the literature measured with the Nujol and KBr pellet methods [42, 43]. The IR reflectance spectrum of the glass shows a broad peak of asymmetric SiO stretching vibration at 960 cm^{-1} with a broad shoulder at 1150 cm^{-1} [44]. There is considerable disagreement about the origin of this shoulder in the case of vitreous SiO_2 in the literature (see, e.g., [45 - 50]). However, when the spectra of crystalline and glassy spodumene are compared, it seems that the shoulder in the spectrum of the glass corresponds to the peaks visible in the spectrum of crystalline spodumene. The respective peaks in the spectrum of crystalline spodumene might be broadened by additional disorder in the glass. When the crystalline sample is ball milled the peak at 1150 cm^{-1} is broadened indicating partial amorphization. The most important difference between the spectra of glassy and crystalline spodumene is the shift of the main peak from 990 cm^{-1} in crystalline spodumene to 960 cm^{-1} in glassy spodumene. The chemical composition and the structural subunits (coordination polyhedra) of glassy spodumene and crystalline β-spodumene are identical (see above and e.g. [40, 41]). In both cases, Al as well as Si are tetrahedrally coordinated. Therefore, the shift of the SiO asymmetric stretching vibration might be attributed to contributions of smaller Si-O-Si bond angles in the bond angle distribution in the glass [45, 51, 52, 53]. In crystalline β-spodumene, rings of 5, 6, and 7 tetrahedra exist in the network [28]. In the glass also smaller and larger rings do exist [54]. Interestingly, when the glassy sample is ball-milled, this peak is shifted to higher wave numbers (980 cm^{-1} after 4 h in a ZrO_2 vial set) thus converging to the value found for crystalline spodumene. For vitreous SiO_2, a direct correlation between the maximum of the SiO stretching vibration peak and the so-called fictive temperature [66], at which the structure is frozen, was shown [52, 53]. Here, a larger Si-O-Si bond angle is associated with a decrease of the fictive temperature. So the shift of the maximum of the IR peak we observed during milling the spodumene glass might as well be due to a reduction of the fictive temperature, i.e. structural relaxation. An IR study on structural relaxation in spodumene glass due to thermal annealing was recently published in Ref. [55].

In the case of $LiBO_2$, the IR spectra (see Fig. 7b) of the crystalline and glassy samples show considerable differences reflecting the different coordination poly-

hedra present in the crystal and in the glass. The structure of crystalline α-$LiBO_2$ consists of metaborate chains which are made up of trigonal BO_3 units with two bridging oxygen atoms and one oxygen atom not being part of the chain. The resulting negative charge of the chains is compensated by the Li ions. The IR spectrum of the crystalline sample (Fig. 7b, bottom) is composed of the bands typical of α-$LiBO_2$ (marked by dark circles; 1430 cm^{-1} and 1150 cm^{-1}: B-O stretching vibration of trigonal BO_3 units, 730 cm^{-1} and 635 cm^{-1}: deformation of the borate chain, 550 cm^{-1}: Li vibration in the lattice) and those of γ-$LiBO_2$ (marked by asterisks) with the vibration bands of tetrahedral BO_4 units around 1000 cm^{-1} [30, 56]. The IR spectrum of the glass (see Fig. 7b, top) shows broad bands of both tetrahedral BO_4 units (around 1000 cm^{-1}) and trigonal BO_3 units (1440 cm^{-1} and 1240 cm^{-1}), the deformation vibration at 730 cm^{-1} and the Li vibration at 460 cm^{-1}. During milling of the glass, the spectrum is not altered very much indicating that the local structure is only slightly changed. However, also for glassy $LiBO_2$ the peak at 950 cm^{-1} is increased in relative intensity and shifted a little bit to higher values (970 cm^{-1}) during milling which, again, indicates slight structural changes. For the microcrystalline sample the situation is quite different. While the bands of γ-$LiBO_2$ are not changed in intensity during milling (as similarly found in XRD), the typical bands of α-$LiBO_2$ decrease in intensity. Obviously, α-$LiBO_2$ is turned into amorphous $LiBO_2$. The vibration bands for trigonal BO_3 are shifted to the values typical of the glass. Most importantly, some of the BO_3 units are transformed into tetrahedral BO_4 units forming a broad band around 1000 cm^{-1} as found in the glass. Except for the residual peaks (about 7%) of α-$LiBO_2$ and those of γ-$LiBO_2$, the IR spectrum of the nanocrystalline sample is identical to that of the nanoglassy sample or the glass. Thus, the nanocrystalline sample consists of nanocrystals embedded in an amorphous matrix (cf. the DTA results shown in Fig. 2). The results found by IR spectroscopy are corroborated by ^{11}B MAS NMR measurements (see Fig. 8b). The spectrum of the crystalline sample is composed of two main contributions. Firstly, a narrow line around 0 ppm (w.r.t. $BF_3 \cdot Et_2O$) which represents tetrahedral BO_4 units of γ-$LiBO_2$ and, secondly, a broad line around 10 ppm which represents trigonal BO_3 units [57]. During milling, the amount of tetrahedral BO_4 is increased. The spectra of the glassy, nanoglassy and nanocrystalline samples are nearly identical. Here, the relative amount of tetrahedral BO_4 is slightly above 40% which is the value also reported in the literature [58].

3.5 Interpretation of the findings

As found here as well as in other glass forming systems, the diffusivity of the glass is higher than that of the corresponding crystal [13, 14, 16, 17, 19, 20]. This can be attributed to two main effects. Firstly, the structural units are not uniform like in a crystal but disordered. There exists a distribution of bonding angles, ring statistics and bond lenghts resulting in a distribution of activation energies for an ion which performs jumps in the glass network [59, 60, 40, 61].

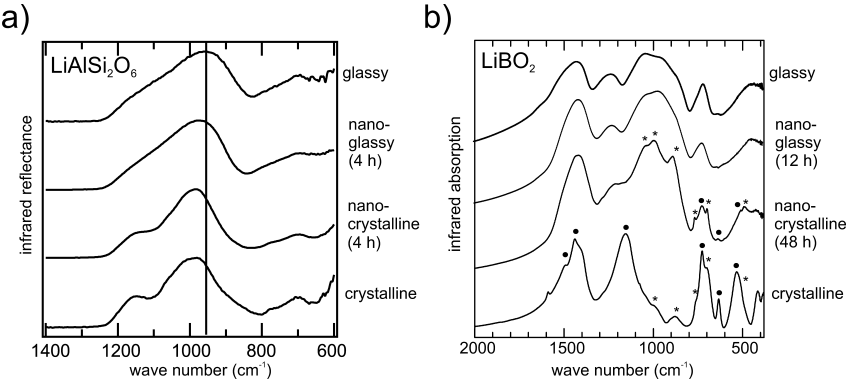

Fig. 7. a) IR reflectance spectra of microcrystalline, nanocrystalline, nanoglassy and glassy $LiAlSi_2O_6$. The vertical line at 960 cm^{-1} shows the shift of the peak during milling of the glass. b) IR absorption spectrum of microcrystalline, nanocrystalline, nanoglassy and glassy $LiBO_2$. Dark circles denote vibration bands of α-$LiBO_2$, asterisks denote those of γ-$LiBO_2$ (see text).

Percolation of low-potential barriers leads to highly diffusive pathways which determine the over-all diffusivity [62, 63]. Secondly, the density of a glass is usually 1–2% lower than that of the crystal since the structure of the glass refers to a high-temperature equilibrium structure of the liquid. There are defects or local strains of very high enthalpy present. Although this is not necessarily the case, this can promote the diffusivity of ions diffusing through the network.

The diffusivity in the two crystalline materials studied here is enhanced by HE ball milling. This effect has also been found for other ion conducting materials (see, e.g., [10, 26, 64, 65, 66]) and is attributed to highly defective or amorphous grain boundaries introduced into the sample in mechanical treatment. As the crystallite size is reduced these highly diffusive grain boundaries more and more dominate the over-all properties of the whole sample (see section 1). However, the diffusivity of the glass is not reached even though sometimes, as in the present case, amorphization takes place. This might be due to the fact that the structure of the glass refers to a very high fictive temperature, at which the structure is frozen [66]. In mechanical treatment, it is rather improbable that a glass-like structure refering to a high-temperature equilibrium state with its high free volume and local strains is produced. Only structures that are stable under the conditions present in the mill can be produced by milling. This is obviously not the case for the as-quenched glassy structure since it is indeed changed during milling. The decrease of diffusivity in the glass in mechanical treatment is an effect that has, to our knowledge, not been observed before. On first sight it seems astonishing that in the one case HE ball milling increases the diffusivity while in the other case a decrease of diffusivity is found. Our structural investigations show no structural change concerning the coordination sphere that could be responsible for the decrease of diffusivity when going from the glass to the

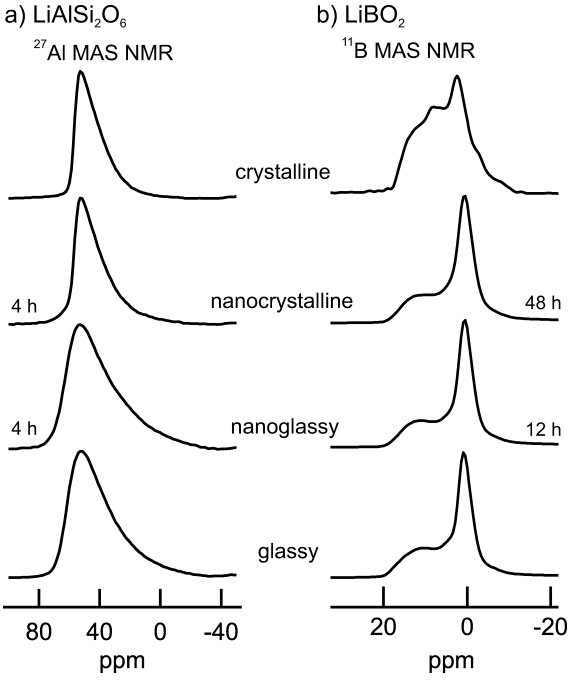

Fig. 8. a) ^{27}Al MAS NMR spectra of crystalline, nanocrystalline, nanoglassy and crystalline $LiAlSi_2O_6$ recorded at 104.3 MHz with a rotating frequency of 10 kHz. The nanostructured samples shown here were milled in a zirconia vial. b) ^{11}B MAS NMR spectra of crystalline, nanocrystalline, nanoglassy and crystalline $LiBO_2$ recorded at 128.3 MHz with a rotating frequency of 10 kHz.

nanoglass. It seems that only slight structural changes are responsible for this decrease of diffusivity. The shift of IR bands corresponding to the silicate and borate network, respectively, indicate that this slight change might be a structural relaxation. If we consider the picture of statistical, chaotic high-energy impact on the material to be ground again and imagine what could happen to a glass with its structure far away from room-temperature equilibrium, it is not surprising that the energy transferred by the impact provokes the structure to relax. Structural relaxation in glasses is a well known phenomenon which can be induced by annealing at a temperature below the glass transition temperature T_g or in mechanical treatment (see, e.g., Refs. [67, 68, 55, 69]).

4. Conclusion

Li diffusion in two glass forming model systems was studied. The influence of high-energy ball milling on the diffusivity was examined for both crystalline and

glassy samples. In case of the crystalline samples, an increase of diffusivity was found, while in the glassy samples, the diffusivity was decreased during milling. The diffusivities of the ball milled crystalline and glassy samples approach each other. The convergence effect was verified using both short-range and long-range sensitive methods. A possible structural concept explaining the findings is proposed. The increase of diffusivity in the crystalline sample is due to the formation of amorphous grain boundaries. The decrease of diffusivity in the glassy sample might be due to structural relaxation. The structure of the glass is comparable to the equilibrium structure of the liquid at elevated temperatures. In mechanical treatment, the structure might relax to a state nearer to equilibrium. The structure of this relaxed glass is supposed to be similar to that of the amorphous grain boundaries produced by HE ball milling in the crystalline materials. The proposed structural model is corroborated by IR spectroscopy and MAS NMR spectroscopy measurements.

Acknowledgement

We are grateful to Martin Wilkening, Armin Feldhoff, Claus Rüscher, and Andre Düvel for help and fruitful discussions and thank the DFG for financial support.

References

1. *Nanostructured Materials: Processing, Properties, and Applications.* C. C. Koch (Ed.), Norwich, NY, William Andrew Pub. (2007).
2. G. Salazar-Alvarez, J. Qin, V. Sepelak, I. Bergmann, M. Vasilakaki, K. N. Trohidou, J. D. Ardisson, W. A. A. Macedo, M. Mikhaylova, M. Muhammed, M. D. Barol, and J. Noguel, J. Am. Chem. Soc. **130** (2008) 13234.
3. C. J. Zhong and M. M. Maye, Adv. Mater. **13** (2001) 1507.
4. C. Xu, J. Tamaki, N. Miura, and N. Yamazoe, Sensors Actuators **B3** (1991) 147.
5. J. V. Stark, D. G. Park, I. Lagadic, and K. J. Klabunde, Chem. Mater. **8** (1996) 1904.
6. P. Greil, Adv. Mater. **14** (2002) 701.
7. M. J. Mayo, Adv. Eng. Mater. **2** (2000) 409.
8. P. G. Bruce, B. Scrosati, and J.-M. Tarascon, Angew. Chem. - Intern. Ed. **47**(16) (2008) 2930.
9. A. S. Aricó, P. G. Bruce, B. Scrosati, J.-M. Tarascon, and W. V. Schalkwijk, Nature Materials **4** (2005) 366.
10. P. Heitjans and S. Indris, J. Phys.: Condens. Mat. **15** (2003) R1257.
11. J. Maier, Nature Materials **4** (2005) 805.
12. H. Gleiter, J. Appl. Cryst. **24** (1991) 79.
13. W. Franke, P. Heitjans, B. Munro, and M. Schrader, in: *Defects in Insulating Materials*. O. Kanert, and J. Spaeth (Eds.), World Scientific Singapore (1993) 1009.
14. W. Franke and P. Heitjans, Ber. Bunsenges. Phys. Chem. **96** (1992) 1674.
15. C. Rüscher, E. Tobschall, and P. Heitjans, in: *Applied Mineralogy in Research, Economy, Technology, Ecology and Culture*. D. Rammlmair, and J. Mederer, Th. Oberthür, R. B. Heimann, and H. Pentinghaus (Eds.), Balkema Rotterdam (2000) 221.
16. P. Heitjans, E. Tobschall, and M. Wilkening, Europ. Phys. J. - Special Topics **161** (2008) 97.

17. F. Qi, R. Böhmer, W. Franke, and P. Heitjans, Phys. Rev. B **72** (2005) 104301.
18. G. Roth and H. Böhm, Solid State Ionics **22** (1987) 253.
19. B. Munro, M. Schrader, and P. Heitjans, Ber. Bunsenges. Phys. Chem. **96** (1992) 1781.
20. R. Winter, P. Siegmund, and P. Heitjans, J. Non-Cryst. Solids **212** (1997) 215.
21. R. Böhmer, P. Lunkenheimer, M. Lotze, and A. Loidl, Z. Phys. B - Condens. Matter **100** (1996) 583.
22. M. Wilkening, A. Kuhn, and P. Heitjans, Phys. Rev. **B 78** (2008) 054303.
23. P. Heitjans, A. Schirmer, and S. Indris, in: *Diffusion in Condensed Matter - Methods, Materials, Models*. P. Heitjans and J. Kärger (Eds.), Springer, Berlin (2005) 369.
24. B. Roling and S. Murugavel, Z. Phys. Chem. **219** (2008) 23.
25. A. Taskiran, A. Schirmeisen, H. Fuchs, H. Bracht, and B. Roling, Phys. Chem. Chem. Phys. **11** (2009) 549.
26. P. Heitjans and M. Wilkening, Def. Diff. Forum **283–286** (2009) 705.
27. A. Kuhn, M. Wilkening, and P. Heitjans, Solid State Ionics **180** (2009) 302.
28. C. T. Li, D. Peacor, Zeitschrift f. Kristallogr. **126** (1968) 46.
29. P. Scherrer, Göttinger Nachrichten **2** (1918) 98.
30. G. D. Chryssikos, E. I. Kamitsos, A. P. Patsis, M. S. Bitsis, and M. A. Karakassides, J. Non-Cryst. Solids **126** (1990) 42.
31. M. Wilkening and P. Heitjans, J. Phys.: Condens. Matter **18** (2006) 9849.
32. J. Waugh and E. Fedin, Sov. Phys. Solid State **4** (1963) 1633.
33. N. Bloembergen, E. Purcell, and R. Pound, Phys. Rev. **73** (1948) 679.
34. S. Indris, P. Heitjans, H. E. Roman, and A. Bunde, Def. Diff. Forum **194–199** (2001) 935.
35. S. Indris, P. Heitjans, H. E. Roman, and A. Bunde, Phys. Rev. Lett. **84** (2000) 2889.
36. M. Wilkening, S. Indris, and P. Heitjans, Phys. Chem. Chem. Phys. **2** (2003) 2225.
37. S. Indris and P. Heitjans, J. Non-Cryst. Solids **307–310** (2002) 555.
38. M. M. Islam, T. Bredow, S. Indris, and P. Heitjans, Phys. Rev. Lett. **99** (2007) 145502.
39. S. Indris, P. Heitjans, M. Ulrich, and A. Bunde, Z. Phys. Chem. **219** (2005) 89.
40. M. C. Jermy, G. N. Greaves, M. E. Smith, G. Bushnell-Wye, A. C. Hannon, R. L., McGreevy, G. Derst, and B. Tilley, Materials Science Forum **228** (1996) 537.
41. A. Nordmann, Y.-B. Cheng, T. J. Bastow, and A. J. Hill, J. Phys.: Condens. Matter **7** (1995) 3115.
42. M. K. Murthy, and E. M. Kirby, J. Am. Ceram. Soc. **45** (1962) 324.
43. M. H. Lin, and M. C. Wang, J. Mater. Sci. **30** (1995) 2716.
44. M. Nocun and M. Handke, J. Mol. Struct. **596** (2001) 139.
45. F. L. Galeener, A. J. Leadbetter, and M. W. Stringfellow, Phys. Rev. B **27** (1983) 1052.
46. R. M. Almeida, Phys. Rev. B **45** (1992) 161.
47. E. I. Kamitsos and A. P. Patis, Phys. Rev. B **48** (1993) 12499.
48. R. M. Almeida, Phys. Rev. B **53** (1996) 14656.
49. E. I. Kamitsos, Phys. Rev. B **53** (1996) 14659.
50. A. A. Stolov and D. A. Simoff, Applied Spectroscopy **62** (2008) 624.
51. A. Agarwal, K. M. Davis, and M. Tomozawa, J. Non-Cryst. Solids **185** (1995) 191.
52. M. Tomozawa, J.-W. Hong, and S.-R. Ryu, J. Non-Cryst. Solids **351** (2005) 1054.
53. S.-R. Ryu and M. Tomozawa, J. Non-Cryst. Solids **352** (2006) 3929.
54. M. Tomozawa, in: *Silicon-based Materials and Devices, Vol 1: Materials and Processing*. H. S. Nalwa (Ed.), Academic Press, San Diego (2001) p. 129.
55. A. Sakamoto and S. Yamamoto, Jpn. J. Appl. Phys. **45** (2006) 6969.
56. K. Nakamoto, *Introduction to Infrared and Raman Spectra of Inorganic and Coordination Compounds* **Part A**, J. Wiley, New York (1997).

57. K. J. D. MacKenzie and M. E. Smith, *Multinuclear Solid-State NMR of Inorganic Materials.* Pergamon/Elsevier, Oxford (2002) p. 428. R-58:Y. H. Yun and P. J. Bray, J. Non-Cryst. Solids **44** (1981) 227.
59. W. Zachariasen, J. Am. Chem. Soc. **54** (1932) 3841.
60. R. Zallen, *The Physics of Amorphous Solids*. J. Wiley, New York (1983).
61. G. N. Greaves and S. Sen, Advances in Physics **56** (2007) 1.
62. A. Bunde, W. Dieterich, P. Maass, and M. Meyer, in: *Diffusion in Condensed Matter - Methods, Materials, Models*. P. Heitjans and J. Kärger (Eds.), Springer, Berlin (2005) 813.
63. R. Zallen and R. Scher, Phys. Rev. B **4** (1971) 4471.
64. P. Heitjans, M. Masoud, A. Feldhoff, and M. Wilkening, Faraday Discussions **134** (2007) 67–82.
65. M. Wilkening, V. Epp, A. Feldhoff, and P. Heitjans, J. Phys. Chem. C **112** (2008) 9291.
66. W. Iwaniak, J. Fritzsche, M. Zukalová, R. Winter, M. Wilkening, and P. Heitjans, Def. Diff. Forum **289–292** (2009) 565.
67. A. Q. Tool, J. Amer. Ceram. Soc. **29** (1946) 240.
68. S. M. Rekhson, J. Non-Cryst. Solids **73** (1985) 151.
69. L. Wondraczek, H. Behrens, Y. Yue, J. Deubener, and G. W. Scherer, J. Am. Ceram. Soc. **90** (2007) 1556.